

# Giant enhancement of attosecond tunnel ionization competes with disorder-driven decoherence in silicon

D. N. Purschke,<sup>\*,1,5</sup> D. Vick,<sup>2</sup> A. Cárdenas,<sup>3</sup> N. Haram,<sup>1</sup> P. Bastani,<sup>1,6</sup> S. Gholam-Mirzaei,<sup>1</sup> S. Mokhtari,<sup>1</sup> V. Jelic,<sup>1</sup> J. Chen,<sup>2</sup> J. Canlas,<sup>2</sup> J. Tordiff,<sup>2</sup> Md. W. Rahman,<sup>2</sup> A. Yu. Naumov,<sup>1</sup> D. M. Villeneuve,<sup>1</sup> A. Staudte,<sup>1</sup> M. Salomons,<sup>2</sup> R. E. F. Silva,<sup>3,4</sup> Á. Jiménez-Galán,<sup>3,4</sup> and G. Vampa<sup>1</sup>

<sup>1</sup>*Joint Attosecond Science Laboratory, National Research Council and University of Ottawa, Ottawa, Ontario K1N 5A2, Canada*

<sup>2</sup>*Quantum and Nanotechnologies Research Center, National Research Council, Edmonton, Alberta T6G 2M9, Canada*

<sup>3</sup>*Instituto de Ciencias de Materiales de Madrid, Consejo Superior de Investigaciones Científicas, Madrid 28049, Spain*

<sup>4</sup>*Max-Born-Institut for Nonlinear Optics and Short Pulse Spectroscopy, Berlin D-12489, Germany*

<sup>5</sup>*Present address: Laboratory for Laser Energetics, University of Rochester, Rochester, New York 14623, United States*

<sup>6</sup>*Advanced Laser Light Source, Institut National de la Recherche Scientifique, 1650 Boulevard Lionel-Boulet, Varennes, Québec J3X 1P7, Canada*

E-mail: dpurschk@ur.rochester.edu

## Abstract

High-harmonic generation (HHG) is a strong-field phenomenon that is sensitive to the attosecond dynamics of tunnel ionization and coherent transport of electron-hole pairs in solids. While the foundations of solid HHG have been established, a deep understanding into the nature of decoherence on sub-cycle timescales remains elusive. Furthermore, there is a growing need for tools to control ionization at the nanoscale. Here, we study HHG in silicon along a crystalline-to-amorphous (c-Si to a-Si) structural phase transition and observe a dramatic reshaping of the spectrum, with enhanced lower-order harmonic yield accompanied by quenching of the higher-order harmonics. Modelling the real-space quantum dynamics links our observations to a giant enhancement ( $>250$  times) of tunnel ionization yield in the amorphous phase and a disorder-induced decoherence that damps the electron-hole polarization over approximately six lattice sites. HHG spectroscopy also reveals remnant order that was not apparent with conventional probes. Finally, we observe a rapid and targeted non-resonant laser annealing of amorphous silicon islands. Our results offer a unique insight into attosecond decoherence in strong-field phenomena, establish HHG spectroscopy as a probe of structural disorder, and pave the way for new opportunities in lightwave nanoelectronics.

Solid-state strong-field physics is a growing discipline with applications such as attosecond spectroscopy<sup>1</sup> and lightwave electronics.<sup>2,3</sup> Born from the convergence of attosecond science and condensed matter physics, research in this area aims to use ultrashort laser pulses to measure and control charge injection and motion on a sub-cycle timescale. In semiconductors, a prototypical strong-field process involves the creation of electron-hole pairs by tunnel ionization followed by laser-driven ballistic transport through the crystal lattice. These processes can be monitored via high-harmonic generation (HHG), which is harmonic radiation of free electron-hole pairs undergoing recollision and dynamical Bloch oscillations.<sup>4,5</sup> HHG is thought to be a universal response of matter under illumination by strong fields and has been observed in virtually all classes of solids.<sup>6-10</sup>

A variety of techniques are available to control strong-field processes in solids, for example

using tools from nano-optics to enhance and sculpt fields,<sup>11,12</sup> active modulation with quasi-static fields to break symmetry,<sup>13,14</sup> and control pulses to access new quantum paths<sup>15</sup> and modulate ionization.<sup>16</sup> HHG is also a useful spectroscopic probe, in some cases the electronic dispersion can be extracted from the coherent dynamics of the HHG spectrogram<sup>17</sup> and, furthermore, it can be used to monitor transient phenomena such as light-induced phase transitions and coherent phonons in real time.<sup>18–20</sup> Solids are also the platform of choice for the emerging discipline of attosecond quantum optics.<sup>21</sup>

Comparably few studies have focused on how chemical or structural modifications can be used to control HHG. While theory suggests that HHG can be dramatically enhanced by doping,<sup>22,23</sup> experimental studies have revealed only minor enhancements.<sup>24,25</sup> Furthermore, apart from select studies,<sup>7,8,26</sup> solid-HHG spectroscopy has focused primarily on crystalline (ordered) systems. Amorphous (disordered) solids display a variety of structure motifs and, in the broader materials science community, a significant effort has focused on probing short (1-5 Å) to medium (5-20 Å) range order.<sup>27–29</sup> Trajectories of electron-hole pairs explore the landscape across several nanometers, yet, there has been little investigation into how disorder affects the coherence of electron-hole pairs. More generally, a consensus on the nature of sub-cycle decoherence in solids has not been reached.<sup>30–35</sup>

Here, we show that amorphization of Si driven by a high-dose gallium focused-ion beam (Ga<sup>+</sup> FIB) irradiation reshapes the HHG spectrum and dramatically enhances the efficiency of lower-order harmonics (h5-h11). Simultaneously, the efficiency of h13 and higher are suppressed in amorphous silicon (a-Si) relative to crystalline silicon (c-Si). Our observations are modelled using the semiconductor Wannier equations (SWEs), a real-space approach to quantum dynamics that we show naturally captures the effect of disorder on the coherence of electron-hole pairs.<sup>36</sup> The increased HHG yield is linked to a giant enhancement in the rate of charge injection by tunnel ionization while the quenching of higher-order harmonics is connected to disorder-driven decoherence of electron-hole pairs. We also show that remnant structure from the original crystalline phase manifests in the HHG, indicative of residual

medium-range order, and, furthermore, observe strong-field laser annealing of a-Si islands at low FIB dose. Our work establishes a new framework for understanding dephasing in attosecond dynamics and provides a powerful approach to controlling ionization in silicon on few-nanometer length scales.

## HHG in amorphized silicon

We prepared a-Si films by amorphization of a c-Si substrate using a  $\text{Ga}^+$  FIB. A cross-section of the amorphized surface measured by transmission electron microscopy (TEM) is shown Fig. 1a. The cross-section contains four distinct regions: layer 1 is the c-Si substrate and layer 2 is the amorphized surface. Layers 3-4 are protective caps deposited only for TEM analysis. The TEM images show a sharp transition between the 65 nm thick a-Si layer and c-Si substrate. Characterization of the structure of these layers is provided by three different probes. First, the alternating bright/dark regions in layer 1 are Kikuchi lines, which arise from multiple scattering events and demonstrate the crystallinity of the substrate. This structure is clearly absent in the amorphous layer. Second, convergent-beam electron diffraction (CBED) patterns with an  $\sim 1$  nm diameter electron beam were acquired near the interface of layers 1 (Fig. 1c) and 2 (Fig. 1b) reveal diffraction peaks in the c-Si region but not in the a-Si region, verifying the lack of long-range order. Finally, shown in Fig. 1f are the Raman spectra of the untreated (c-Si) and amorphized (a-Si) samples. The c-Si sample shows a sharp peak at the longitudinal-optical (LO) phonon frequency, while the a-Si sample has additional broad peaks characteristic of a disordered sample. The a-Si also has a residual sharp peak at the c-Si LO frequency, which arises from the c-Si substrate (see Supplementary section Raman spectroscopy for more details).

We excite the surface of a silicon sample with ultrashort pulses from a mid-infrared optical parametric amplifier with a  $3.6 \mu\text{m}$  wavelength and collect the radiation emitted by HHG in reflection geometry, as illustrated in Fig. 1g. Typical HHG spectra with a pump intensity

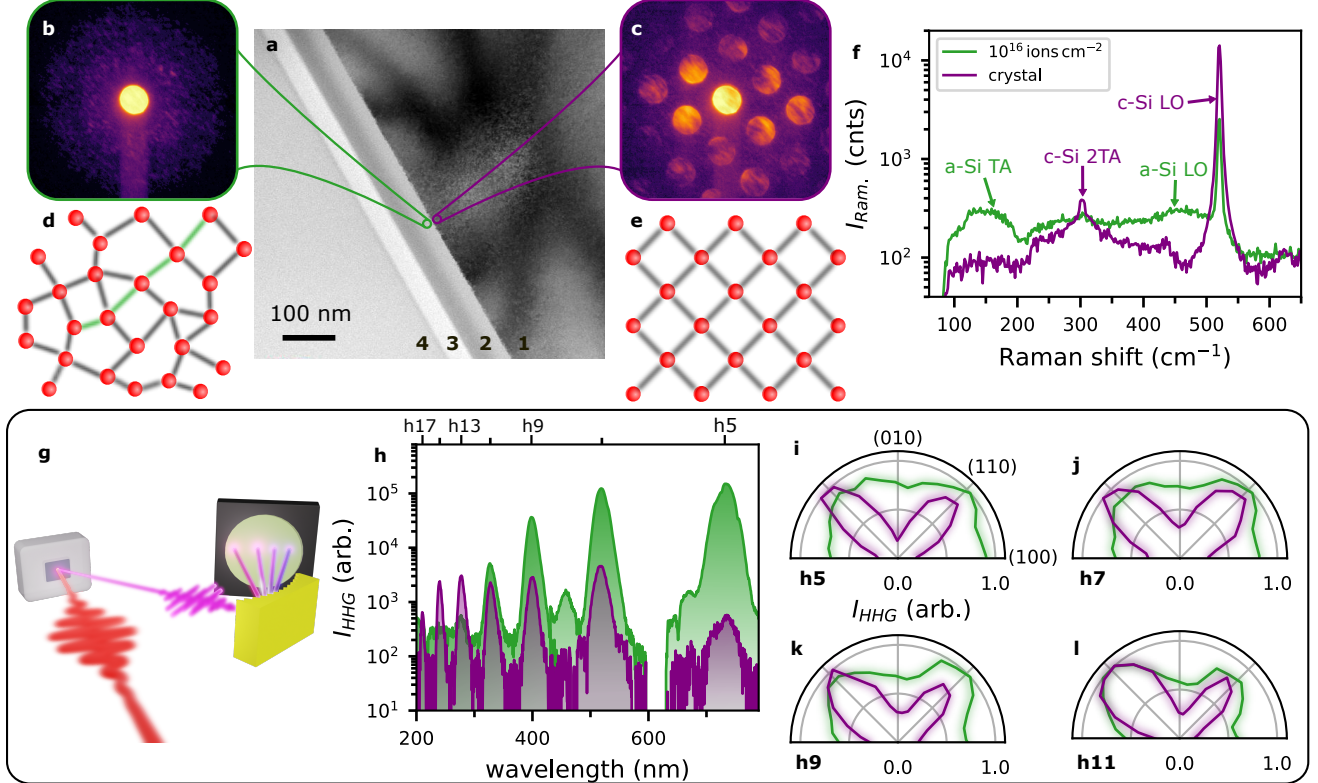


**Fig. 1: HHG in a-Si vs c-Si.** **a**, TEM micrograph showing the cross-section of an amorphized region of the Si surface. Numbers indicate the 1: c-Si substrate, 2: a-Si film, 3-4: protective carbon layers deposited prior to lamella milling. Log-scaled colormap of the CBED patterns with the electron beam focused on **b**, the amorphized silicon layer and **c**, the crystalline silicon substrate. Illustrations of **d**, the amorphous and **e**, crystalline structures at the atomic scale. The green bond lines illustrate the residual medium-range order aligned with the original cubic structure. **f**, Raman spectra measured in reflection mode with a 633 nm excitation wavelength for an unexposed (purple) and an amorphized (green) region of the silicon wafer. **g**, Schematic layout of the experimental apparatus for measuring HHG radiation. Relative to **a**, the laser is incident from left to right on layer 2 and harmonics are collected in reflection. **h**, Experimentally measured HHG signal for the crystalline (purple) and amorphized (green,  $5 \times 10^{15} \text{ cm}^{-2}$  ion dose) regions of the Si surface at a peak laser intensity of  $360 \text{ GW} \cdot \text{cm}^{-2}$ . **i-l**, Polarization-dependent HHG yield for harmonics h5-h11, respectively, for c-Si (purple) and a-Si (green).

of  $360 \text{ GW} \cdot \text{cm}^{-2}$  are shown for a-Si (green) and c-Si (purple) in Fig. 1h. Amorphization leads to a significant reshaping of the HHG spectrum, with a surprising enhancement in yield of lower-order harmonics (h5-h11) in a-Si relative to c-Si. The enhancement is particularly dramatic for h5, which shows an  $\sim 500$ -fold increase in yield at this laser intensity. Simultaneously, the cutoff harmonic order is reduced and higher-order harmonics are quenched.

The dependence of the HHG yield on polarization of the incident laser, which is sensitive to the underlying crystal symmetry,<sup>37-39</sup> is also modified by amorphization. The polar plots in Fig. 1i-l show that amorphization reduces the modulation depth in the lobe structure for harmonics h5-h11. Interestingly, all harmonics retain some signature of the original c-Si cubic structure; this remnant structure becomes more prominent for increasing harmonic orders. Note that it cannot arise from the c-Si substrate: for lower-order harmonics, this is apparent from the enhancement in yield, while for higher-order harmonics, the 65 nm a-Si film thickness is sufficient to reabsorb emission from the c-Si substrate (the penetration depth for 350 nm light is  $\sim 10$  nm). This indicates that the residual medium range order in the amorphized film remains preferentially aligned with the original crystal axis. In contrast, this polarization-dependent structure is not present in the HHG spectra of evaporated a-Si films (Extended Data Fig. 3), where there may be medium-range order but with no preferred orientation. Note that this remnant order was not apparent in TEM, CBED, or Raman measurements.

## Disorder in attosecond quantum dynamics

As illustrated in Figs. 2a-b, amorphization has two effects on the energy landscape, which are in competition in the reshaping of the HHG spectrum. First, the direct gap is reduced from 3.5 eV in c-Si to approximately 1.75 eV in a-Si.<sup>40</sup> This leads to an increased charge injection by tunnel ionization, thereby enhancing the HHG yield. Second, disorder introduces irregularity in the energy landscape.<sup>41,42</sup> In a semiclassical picture, for the class of so-called

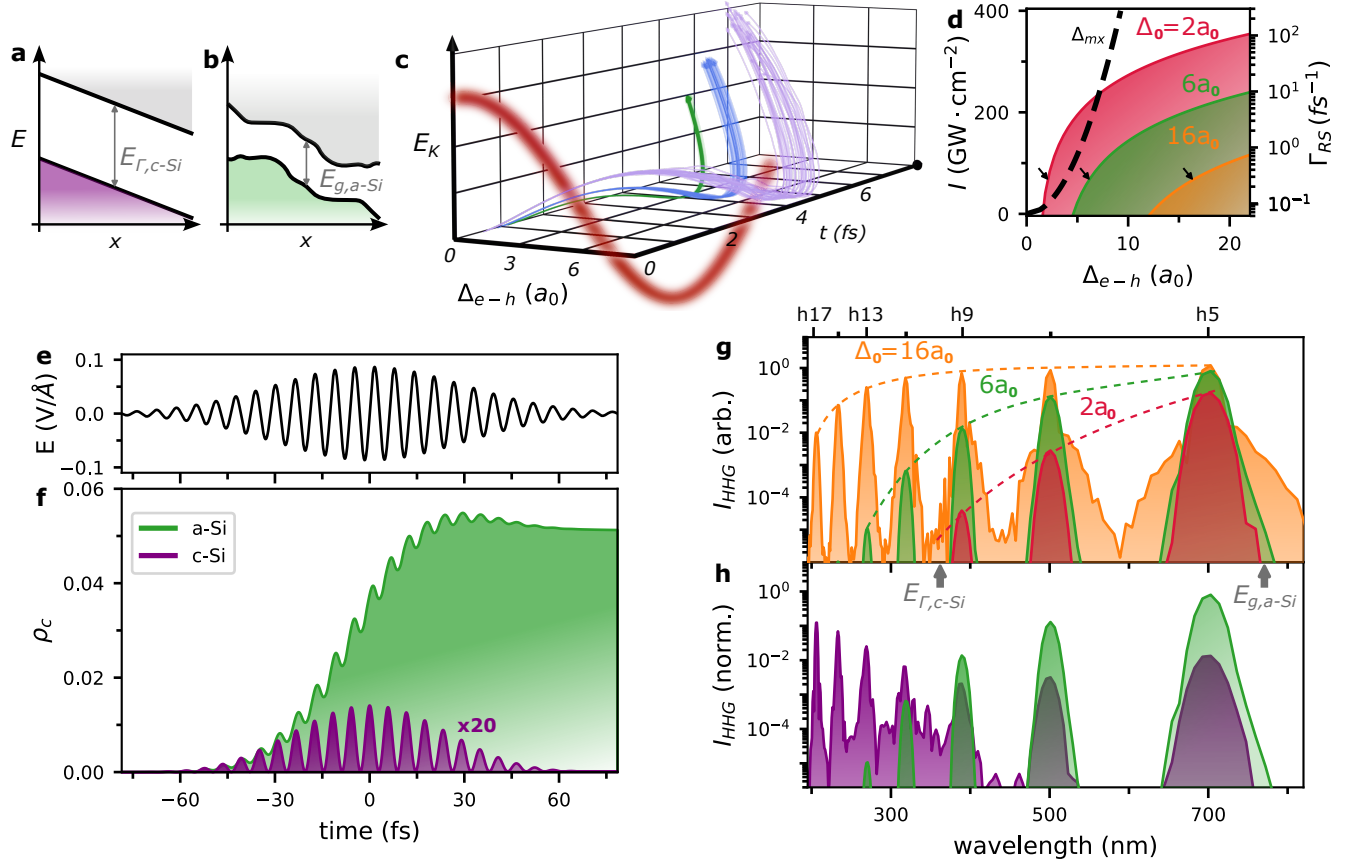


**Fig. 2: Role of disorder in attosecond quantum dynamics.** Schematic illustration of the tunneling barrier in a strong electric field for **a**, c-Si and **b**, a-Si. **c**, Trajectory picture of HHG in a disordered crystal, where longer trajectories explore more of the inhomogeneous energy landscape, which randomizes their return time and energy. **d**, Parameterizations of the real-space dephasing (colored/shaded areas) used in **g** and semiclassical estimate of the the peak electric field required for the electron-hole excursion to reach  $\Delta_{e-h}$  (black curve). The black arrows indicate the point where the dephasing rate reaches a third of a cycle, i.e.,  $\Delta_0$ . **e**, Electric field and **f**, the corresponding population density calculated for a-Si (green) and c-Si (purple). **g**, Spectra calculated from the SWEs using a 1D model with a 1.75 eV band gap with real-space dephasing rates given by the curves in **d**. **h**, Spectra calculated with the same model as in **g**, but comparing c-Si (purple, gap 3.5 eV and  $\Delta_0 = 16a_0$ ) and a-Si (green, gap 3.5 eV and  $\Delta_0 = 6a_0$ ). The peak intensity was  $340 \text{ GW} \cdot \text{cm}^{-2}$  in each calculation.

short trajectories, which most accurately describe solid HHG,<sup>4</sup> higher-order harmonics have longer excursions and probe the irregular energy landscape over larger distances. In Fig. 2c, we plot an ensemble of closed trajectories for several birth times with a random scattering rate that increases with increasing separation, illustrating both the attochirp and the order-dependent excursion length.<sup>30</sup> Disorder randomizes the return time and energy of longer trajectories, which preferentially quenches higher-order harmonics. For the highest intensities, we estimate a maximum excursion length beyond 7 lattice sites, which is facilitated by the mid-infrared pump wavelength. The long-wavelength pump also allows us to explore larger volumes while minimizing the role of higher-lying conduction bands, which complicates the trajectory picture and obscures the signature of disorder in the HHG spectrum.<sup>7</sup>

To corroborate this picture and to be more quantitative, we develop a model of the attosecond quantum dynamics in a-Si using the framework of the SWEs.<sup>36</sup> In contrast to the commonly used semiconductor Bloch equations, coherences in the SWEs are tracked in real space. We exploit this to capture disorder-induced decoherence using a real-space dephasing rate,  $\Gamma_{RS}$ , that smoothly turns on with increasing electron-hole separation,  $\Delta_{e-h}$ , as shown in Fig. 2d. While real-space dephasing has previously been used as a tool to mimic macroscopic propagation,<sup>35</sup> we show that it can be linked to *microscopic physics* that, in the case of a-Si, dominates the yield of the higher-order harmonics.

The SWEs were solved separately in 1D for model systems with 2-bands and band gaps equal to those of a-Si and c-Si, respectively. As shown in Fig. 2f (see also log-scaled plots in Extended data Fig. 2), the reduction in band gap leads to an enormous enhancement in the ionization yield, which is responsible for the enhancement of low-order harmonic generation. Simultaneously, Fig. 2g shows that the roll-off in the HHG spectra is extremely sensitive to the location of the real-space dephasing boundary,  $\Delta_0$  (defined by  $\Gamma_{RS}(\Delta_0) = 3\omega_0$ ). With this definition, only the fine structure of the HHG spectra are sensitive to the curvature of  $\Gamma_{RS}$  (see Supplementary section Role of real-space dephasing in quantum dynamics). This provides us an estimate of the length scale over which electron-hole coherence is lost;

heuristically, we associate  $\Delta_0$  as the length scale over which medium-range order exists and the energy landscape can be considered approximately smooth. From Fig. 2g, we see that  $\Delta_0 \approx 6a_0$ , where  $a_0 = 0.543 \text{ \AA}$  is the c-Si lattice constant, provides the best agreement with the experimentally measured HHG spectrum. For comparison, we also plot the HHG spectra calculated for c-Si along side that of a-Si in Fig. 2d.

## Mapping the structural phase transition

With this understanding in hand, we can explore the connection between amorphization and HHG further by studying the role of Ga-implantation dose on the harmonic yield. The dose was varied by over 4 orders of magnitude, ranging from  $4 \times 10^{12} \text{ cm}^{-2}$  to  $4 \times 10^{16} \text{ cm}^{-2}$ . Note that the dose reported by Sivis et al. (ref. 24) was just  $3 \times 10^{12} \text{ cm}^{-2}$  and the reported yield enhancement was small (Fig. S7 in ref. 24). As shown in Fig. 3a, up to  $10^{14} \text{ cm}^{-2}$  the yield of h5 increases before plateauing at  $10^3$  times higher than the pure crystalline substrate. The onset of this plateau coincides remarkably well with reported values of the critical dose required for complete amorphization by Ga-FIB.<sup>43,44</sup> At lower doses, the structure consists of amorphous islands within a crystalline background as opposed to a fully amorphous film.<sup>45</sup> In contrast to h5, the yield of h13 drops off as the Ga dose increases, however, the behavior is not monotonic. For samples above the critical dose, a noisy background/continuum generation made it more difficult to measure these harmonics (Extended Data Fig. 1e).

In Fig. 3b, we study the pump-intensity-dependent yield of the fifth harmonic for samples near the critical dose. Below  $200 \text{ GW} \cdot \text{cm}^{-2}$ , all samples show an increased yield relative to c-Si. The pump intensity was increased up to the laser-induced damage threshold (LIDT), which was accompanied by visible damage and a pronounced drop in HHG yield. At the a-Si LIDT, which dropped with increasing ion dose (see Extended Data Fig. 4), the  $3.1 \times 10^{14} \text{ cm}^{-2}$  sample was 250 times brighter than c-Si at the same intensity and 10 times brighter than c-Si at its own LIDT. The slope of the intensity scaling of the lower-dose sam-

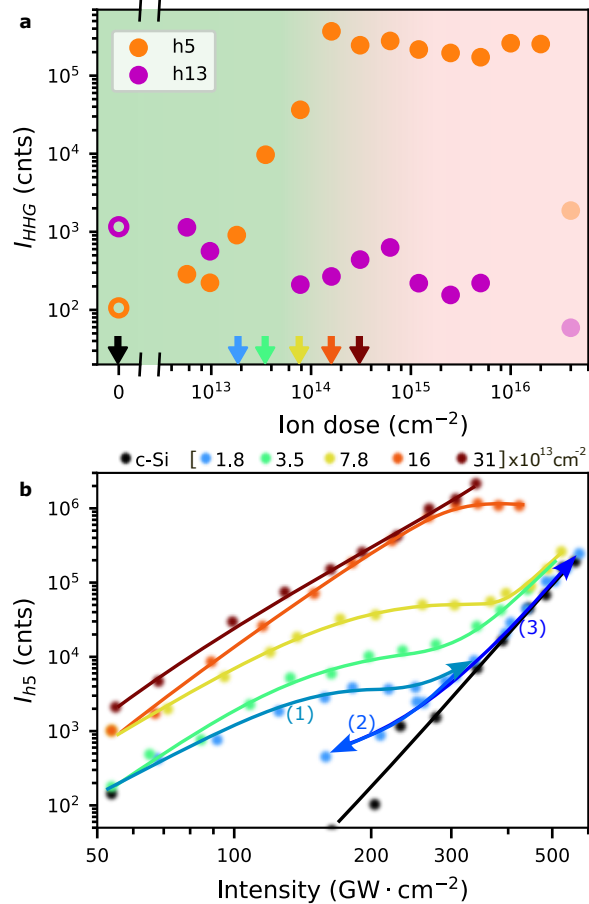


**Fig. 3: Mapping the structural phase transition.** **a**, Yield of the 5<sup>th</sup> (orange circles) and 13<sup>th</sup> (magenta circles) harmonics with a  $210 \text{ GW} \cdot \text{cm}^{-2}$  peak laser pulse intensity for samples of varying ion dose. The green to red transition indicates the approximate critical dose based on expectation from literature. The data point at  $2 \times 10^{16} \text{ cm}^{-2}$  is faded because this fluence was above the damage threshold for this sample (Extended data Fig. 4). **b**, Yield of the 5<sup>th</sup> harmonic as a function of laser intensity. All samples were measured up to the damage threshold. The solid lines are smoothed curves to highlight the trends in data. The blue lines labeled (1-3) with arrows indicate the direction that the intensity was scanned for this sample, revealing an irreversible reduction in yield after exposing the sample to high intensities without visible damage. The ion doses in the legend are measured in units of  $10^{13} \text{ cm}^{-2}$ . The arrows in **a** are color-coded to match the corresponding samples in **b**.

ples develop a shoulder in the HHG yield at approximately  $210 \text{ GW} \cdot \text{cm}^{-2}$  and the yield is nearly flat with intensity. For the  $1.8 \times 10^{13} \text{ cm}^{-2}$  sample, we traced the yield as a function of intensity in three steps: (1) from 0 to  $320 \text{ GW} \cdot \text{cm}^{-2}$ , (2) down to  $180 \text{ GW} \cdot \text{cm}^{-2}$ , (3) up to  $550 \text{ GW} \cdot \text{cm}^{-2}$ . From step (1) to (2), we observe an irreversible reduction in yield, however, as is apparent from step (3), we did not yet damage the sample. In fact, the yield and LIDT at high intensities is the same as c-Si. All samples with dose  $\leq 16 \times 10^{13} \text{ cm}^{-2}$  showed this behavior, which, in the following section, we show is due to laser annealing.

## Laser annealing via tunnel ionization

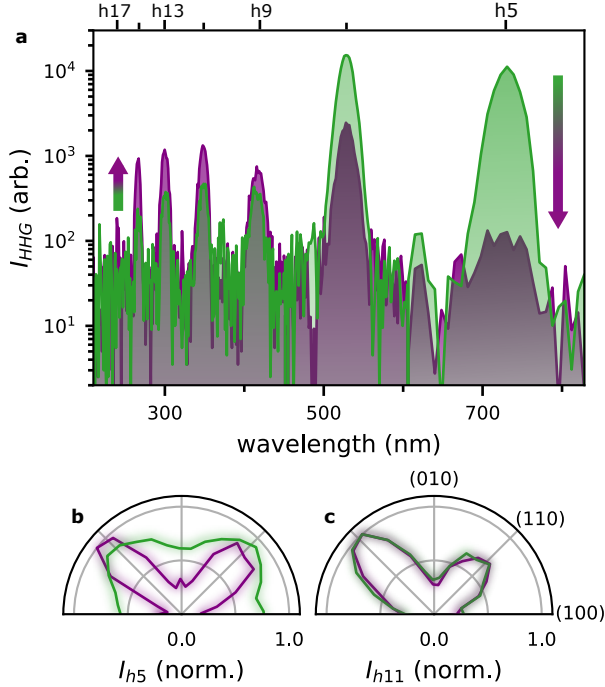


**Fig. 4: Laser annealing by tunnel ionization.** **a**, Harmonic spectrum before (dark red) and after (purple) laser annealing. Spectra were acquired with a peak laser intensity of  $190 \text{ GW} \cdot \text{cm}^{-2}$  and the sample was annealed with a peak laser intensity of  $440 \text{ GW} \cdot \text{cm}^{-2}$ . Yield of the  $5^{\text{th}}$  harmonic **b**, and the  $11^{\text{th}}$  harmonic **c**, as a function of laser polarization relative to the crystal axes of the bulk (unexposed) silicon crystal for the same laser intensity as in **a**.

The HHG spectrum at a laser intensity of  $190 \text{ GW} \cdot \text{cm}^{-2}$  (green curve in Fig. 4) was measured in a sample with  $3.5 \times 10^{13} \text{ cm}^{-2}$ , i.e., below the critical dose. Subsequently, we

increased the laser intensity to  $440 \text{ GW} \cdot \text{cm}^{-2}$  and exposed the film for approximately 20 seconds. The HHG spectrum was measured again (purple curve in Fig. 4a), demonstrating a significant reduction in the yield of lower-order harmonics (h5,h7) accompanied by an enhancement in the yield of higher-order harmonics (h9-h17). Furthermore, as seen in Fig. 4b, the polarization dependence of h5 shows a significant increase in the modulation depth, indicating that laser annealing heals the crystal structure. Curiously, as shown in Fig. 4c, the modulation depth of h11 resembles that of c-Si and is not affected by annealing. Notably, the spectrum in Fig. 4a shows a plateau-like structure in the higher-order harmonics but with a decreased yield relative to c-Si. In contrast to the sample studied in Fig. 1, here the Ga dose was kept below the threshold for amorphization where a-Si islands are formed in the c-Si background. The higher-order harmonic emission selectively probes the c-Si regions while low-order harmonic emission is more sensitive to the emerging a-Si islands.

Importantly, these observations allow us to verify that the enhanced HHG yield we observe is linked to the amorphization of the structure as opposed to Ga impurity states (we estimate a Ga concentration on the order of  $10^{19} \text{ cm}^{-3}$  near the critical dose - see Extended Data Fig. 5). Furthermore, in contrast to more conventional annealing techniques (thermal, electron beam, or resonant laser annealing) energy deposition via tunnel ionization preferentially targets the amorphous islands with reduced band gap. It also has the advantage of being able to efficiently transmit through thick substrates. Further exploration of this novel mechanism for laser annealing using intense non-resonant lasers is therefore warranted. Finally, these HHG imaging, where spatial resolution is limited only by the harmonic cutoff wavelength,<sup>46</sup> could be a useful probe of mesoscopic structural disorder.

## Conclusion

To conclude, our results transform our understanding of sub-cycle decoherence in solids and reveal a new avenue for enhancing tunnel ionization in silicon. Our approach could be used

to create a-Si patterns on few-nanometer length scales, enabling the fabrication of nanoscale circuit elements for lightwave electronics. While here we pattern a-Si regions using FIB, the underlying control mechanism (amorphization by ion implantation) is CMOS compatible. Furthermore, our work points to new opportunities for hybrid structures exploiting, e.g., both plasmonics and nano-patterned a-Si. The enhancement of ionization comes at the cost of increased decoherence, which is imprinted into the roll-off of the HHG spectrum. This allows us to probe medium-range order on a deeply sub-wavelength scale, which evokes a ballistic-transport analogy to time-resolved terahertz spectroscopy, where carrier localization in diffusive transport is imprinted onto the conductivity spectrum.<sup>47,48</sup> We expect our approach to spur new exploration into the nature of attosecond decoherence arising from dynamical disorder, such as phonons and zero-point motion, and find application in the study of liquid-phase attosecond quantum dynamics.<sup>49,50</sup>

## Methods

### HHG Spectroscopy

As shown in Extended Data Fig. 6, a 100 kHz Yb-based laser amplifier system (Light Conversion, Carbide CB3-80, 0.8 mJ pulse energy) pumps a mid-infrared optical parametric amplifier (Light Conversion, Orpheus MIR) to generate ultrashort pulses of  $3.6 \mu\text{m}$  wavelength and approximately 50 fs duration. Further details of the system are provided in ref. 51. Optical harmonics are generated from a silicon surface and collected in reflection mode. The harmonic radiation is focused into a spectrometer consisting of a UV grating (McPherson) and intensifier with an S20UV photocathode (Photonis). The grating was rotated to capture spectra at different central wavelengths; three different settings are required to capture the HHG spectrum from h5-h17. The third harmonic was not measured as the intensifier is not sensitive to the 1200 nm wavelength. The system is not sensitive to the nineteenth harmonic and higher ( $\lambda \leq 190 \text{ nm}$ ) due to the  $\sim 2 \text{ m}$  propagation length in air and UV-Al routing

mirrors (not shown in schematic). However, we note that c-Si likely supports emission of these harmonics at the intensities used here.<sup>39</sup>

Peak laser intensities,  $I$ , were calculated using the expression for the total energy,  $U$ , of a Gaussian pulse as,

$$I = \frac{4 \ln 2}{\pi^{3/2} w \tau} U \cdot T \quad (1)$$

where  $w$  is the  $e^{-2}$  beam radius ( $\sim 30 \mu\text{m}$ ),  $\tau$  is the FWHM pulse duration ( $\sim 50 \text{ fs}$ ), and  $T$  is the transmission coefficient at the air/Si interface given by,

$$T = 1 - \frac{(n - 1)^2}{(n + 1)^2}, \quad (2)$$

with  $n = 3.4$  the refractive index of silicon at  $3.6 \mu\text{m}$ . Note that the refractive index of a-Si and c-Si are similar in the MIR.<sup>52</sup>

## Ion implantation

The ion implantation experiments were conducted on a Zeiss NVision 40 dual beam microscope in which 30 keV Ga<sup>+</sup> ions were focused onto a weakly n-doped silicon (100) substrate. An array of write fields of dimension  $410 \mu\text{m} \times 340 \mu\text{m}$  were exposed to create ion fluence conditions spanning the range  $2 \times 10^{12} - 4 \times 10^{16} \text{ ions} \cdot \text{cm}^{-2}$ . The write fields were separated by 4 mm and marked with ion-milled fiducials at the write-field corners to facilitate ease of identification and alignment during the subsequent optical interrogation experiments. In order to produce ion fluence conditions spanning 4 orders of magnitude, two parameters were varied: the ion beam current (selected from 40 pA, 150 pA, 705 pA, and 6400 pA); and the total exposure time. One additional adjustment was done in order to ensure a laterally uniform exposure: the objective lens of ion column set to an underfocus condition to produce a beam spot diameter of  $3 \mu\text{m}$ ; this ensured that the ion beam overfilled the 186 nm pixel size of the raster pattern. All beam current settings were verified by means of a Faraday Cup prior to performing the exposures.

## Electron microscopy and elemental analysis

Site-selected lamella samples were prepared in a Hitachi NB5000 FIB. Lamellae sites were selected within and immediately outside a write field of ion dose  $4 \times 10^{16} \text{ cm}^{-2}$ . A third lamella was prepared from the centre of a laser interrogation site situated within the same write field. Prior to FIB milling of the lamella, the substrate was sputter coated with a carbon layer of thickness 40 nm (layer 3 in Fig. 1a). This step created a separation layer that allowed the Ga of the implantation layer to be readily distinguished from the additional Ga introduced during the preparation of the TEM sample in the FIB, which includes a gas-injection system (GIS) assisted 2  $\mu\text{m}$  thick Ga-rich carbon coating (layer 4 in Fig. 1a).

The CBED was performed under scanning-TEM mode with a JEOL 2200FS TEM at an accelerating voltage of 200kV. The beam convergence angle for the CBED pattern collection is 2.5 mrad and the electron beam waist is 1 nm at the focus. Elemental maps were acquired on a JEOL JEM-ARM200CF transmission electron microscope equipped with a with large angle silicon drift detector energy dispersive spectrometer. Extended Data Fig. 5a shows a Dark field (DF) image in the vicinity of the sample surface. For comparison, a portion of a DF image from the non-implanted sample is shown in frame Extended Data Fig. 5b. Elemental maps of Si, Ga, and O were collected from the area shown in frame, background subtracted and integrated parallel to substrate surface to obtain the plots shown in Extended Data Fig. 5c. The profiles indicate that the majority Ga ions are implanted within 65 nm from the surface, along with a corresponding drop in the Si signal in this layer. Note that the ion fluence in this sample was 200 times that of the critical dose. Additionally, In addition to the Ga, an O signature was observed at the surface of both implanted and non-implanted samples, indicative of a native oxide layer.

## Semiconductor Wannier equations

To capture the essential physics, we employ a minimal tight-binding one-dimensional chain with two orbitals per unit cell separated by a distance  $a/2$ , where  $a$  is the unit cell vector

of c-Si ( $a_0 = 5.43$  Å). Both orbitals have different on-site energies, resulting in a band gap of  $E_{g,a\text{-Si}} = 1.75$  eV and  $E_{g,c\text{-Si}} = 3.5$  eV for the a-Si and c-Si, respectively.<sup>40</sup> We solve the semiconductor Wannier equations,<sup>36</sup> i.e., the equations of motion in real space,

$$i\partial_t \rho_{nm}(x, t) = \sum_{x'} \left\{ [h^0(x'), \rho(x - x', t)]_{nm} + E_x(t) [r_x(x'), \rho(x - x', t)]_{nm} \right\} \\ - E_x(t) x \rho_{nm}(x, t) - i\Gamma_{rs}(|\Delta_{nm}|) (\rho_{nm}(x, t) - \rho_{nm}^0(x, t)), \quad (3)$$

in a Bravais lattice vector grid of  $x_{\max} = 50$  sites using a Tsitouras 5/4 Runge–Kutta method with a timestep of  $dt = 0.5$  a.u. Above,  $\rho_{nm}(x', x) = \rho_{nm}(0, x - x') \equiv \rho_{nm}(x - x') = \langle c_{x-x',m}^\dagger c_{0,n} \rangle$  is the reduced density matrix element between orbital  $m$  and orbital  $n$  with relative distance

$$\Delta_{nm} = (x - x')a + (1 - \delta_{nm})\frac{a}{2}, \quad (4)$$

with  $x, x'$  being Bravais vectors of the two sites. The system is described by the periodic crystal Hamiltonian  $h^0(x)$  and the position operator  $r_x(x)$ . The interaction with the electric field  $E_x(t)$  is treated in the dipole approximation and in the length gauge. The high-harmonic spectrum is obtained from the Fourier transform of the current, which itself is computed as,

$$J(t) = |e| \sum_x \sum_{nm} v_{nm}(x) \rho(-x; t), \quad (5)$$

where the velocity operator in one dimension is given by

$$v_{nm}(x) = i \sum_{x'} [r_x(x'), h^0(x - x'),]_{nm} + i x h_{nm}^0(x).$$

In order to reproduce the shorter coherence length of a-Si relative to c-Si, the Wannier approach allows us to use a decoherence term in the equations of motion that depends on the distance between electrons and holes in two orbitals  $n$  and  $m$ ,  $|\Delta_{nm}|$ .<sup>35</sup> We define this

real-space dephasing as,

$$\Gamma_{rs}(|\Delta_{nm}|) = \begin{cases} 0 & |\Delta_{nm}| < \delta_0 \\ \beta (|\Delta_{nm}| - \delta_0)^2 & |\Delta_{nm}| \geq \delta_0 \end{cases} \quad (6)$$

where  $\delta_0$  is the distance at which orbitals start to decohere as a second order polynomial. This functional form was chosen as it is simple and smooth. We define  $\Delta_0$  as the distance at which the dephasing is three times the optical frequency, which sets the curvature as  $\beta = \Gamma_{RS}(\Delta_0)\Delta_0^{-2}$ . We find that the harmonic roll-off is independent on the curvature of  $\Gamma_{RS}$  with this definition of  $\Delta_0$ . See Supplementary info section Role of real-space dephasing in quantum dynamics for further details.

## Acknowledgement

DNP acknowledges funding from the Natural Sciences and Engineering Research Council of Canada (NSERC) Postdoctoral Fellowship Program and the Mitacs Globalink Research Award program. GV acknowledges funding from NSERC Discovery Grant program, Defence Research and Development Canada, and the Joint Center For Extreme Photonics. AJG acknowledges support from the Comunidad de Madrid through TALENTO Grant 2022-T1/IND-24102 and the Spanish Ministry of Science, Innovation and Universities through grant reference PID2023-146676NA-100. The authors wish to acknowledge technical support from R. Kroeker and D. Crane, and L Gaburici for assistance with Raman microscopy.

## References

- (1) Heide, C.; Kobayashi, Y.; Haque, S. R. U.; Ghimire, S. Ultrafast high-harmonic spectroscopy of solids. *Nature Physics* **2024**, *20*, 1546–1557.

(2) Borsch, M.; Meierhofer, M.; Huber, R.; Kira, M. Lightwave electronics in condensed matter. *Nature Reviews Materials* **2023**, *8*, 668–687.

(3) Heide, C.; Keathley, P. D.; Kling, M. F. Petahertz electronics. *Nature Reviews Physics* **2024**, *6*, 648–662.

(4) Vampa, G.; Hammond, T. J.; Thiré, N.; Schmidt, B. E.; Légaré, F.; McDonald, C. R.; Brabec, T.; Corkum, P. B. Linking high harmonics from gases and solids. *Nature* **2015**, *522*, 462–464.

(5) Schubert, O.; Hohenleutner, M.; Langer, F.; Urbanek, B.; Lange, C.; Huttner, U.; Golde, D.; Meier, T.; Kira, M.; Koch, S. W.; Huber, R. Sub-cycle control of terahertz high-harmonic generation by dynamical Bloch oscillations. *Nature Photonics* **2014**, *8*, 119–123.

(6) Yoshikawa, N.; Tamaya, T.; Tanaka, K. High-harmonic generation in graphene enhanced by elliptically polarized light excitation. *Science* **356**, 736–738.

(7) You, Y. S.; Yin, Y.; Wu, Y.; Chew, A.; Ren, X.; Zhuang, F.; Gholam-Mirzaei, S.; Chini, M.; Chang, Z.; , S. High-harmonic generation in amorphous solids. *Nature Communications* **2017**, *8*, 724.

(8) Annunziata, A.; Becker, L.; Murillo-Sánchez, M. L.; Friebel, P.; Stagira, S.; Faccialà, D.; Vozzi, C.; Cattaneo, L. High-order harmonic generation in liquid crystals. *APL Photonics* **2024**, *9*, 060801.

(9) Alcalà, J.; Bhattacharya, U.; Biegert, J.; Ciappina, M.; Elu, U.; Graß, T.; Grochowski, P. T.; Lewenstein, M.; Palau, A.; Sidiropoulos, T. P. H.; Steinle, T.; Tyulnev, I. High-harmonic spectroscopy of quantum phase transitions in a high-T<sub>c</sub> superconductor. *Proceedings of the National Academy of Sciences* **2022**, *119*, e2207766119.

(10) Shima Gholam-Mirzaei; Korobenko, s.; Haram, N.; Purschke, D. N.; Saha, S.; Naumov, A. Y.; Vampa, G.; Villeneuve, D. M.; Silva, R. E. F.; Staudte, A.; Boltasseva, A.; Shalaev, V. M.; Jiménez-Galán, A.; Corkum, P. B. High Harmonic Generation from a Noble Metal. *ArXiv:2503.05073* **2025**,

(11) Ciappina, M. F. et al. Attosecond physics at the nanoscale. *Reports on Progress in Physics* **2017**, *80*, 054401.

(12) Korobenko, A.; Rashid, S.; Heide, C.; Naumov, A. Y.; Reis, D. A.; Berini, P.; Corkum, P. B.; Vampa, G. *In-Situ* Nanoscale Focusing of Extreme Ultraviolet Solid-State High Harmonics. *Physical Review X* **2022**, *12*, 041036.

(13) Vampa, G. et al. Strong-field optoelectronics in solids. *Nature Photonics* **2018**, *12*, 465–468.

(14) Li, S.; Tang, Y.; Ortmann, L.; Talbert, B. K.; Blaga, C. I.; Lai, Y. H.; Wang, Z.; Cheng, Y.; Yang, F.; Landsman, A. S.; Agostini, P.; DiMauro, L. F. High-order harmonic generation from a thin film crystal perturbed by a quasi-static terahertz field. *Nature Communications* **2023**, *14*, 2603.

(15) Purschke, D. N.; Jiménez-Galán, A.; Brabec, T.; Naumov, A. Y.; Staudte, A.; Villeneuve, D. M.; Vampa, G. Microscopic mechanisms of high-order wave mixing in solids. *Physical Review A* **2023**, *108*, L051103.

(16) Roscam Abbing, S. D. C.; Kuzkova, N.; Van Der Linden, R.; Campi, F.; De Keijzer, B.; Morice, C.; Zhang, Z.-Y.; Van Der Geest, M. L. S.; Kraus, P. M. Enhancing the efficiency of high-order harmonics with two-color non-collinear wave mixing in silica. *Nature Communications* **2024**, *15*, 8335.

(17) Vampa, G.; Hammond, T.; Thiré, N.; Schmidt, B.; Légaré, F.; McDonald, C.; Brabec, T.; Klug, D.; Corkum, P. All-Optical Reconstruction of Crystal Band Structure. *Physical Review Letters* **2015**, *115*, 193603.

(18) Bionta, M. R.; Haddad, E.; Leblanc, A.; Gruson, V.; Lassonde, P.; Ibrahim, H.; Chail-lou, J.; Émond, N.; Otto, M. R.; Jiménez-Galán, A.; Silva, R. E. F.; Ivanov, M.; Siwick, B. J.; Chaker, M.; Légaré, F. Tracking ultrafast solid-state dynamics using high harmonic spectroscopy. *Physical Review Research* **2021**, *3*, 023250.

(19) Nie, Z.; Guery, L.; Molinero, E.; Juergens, P.; Van Den Hooven, T.; Wang, Y.; Jimenez Galan, A.; Planken, P.; Silva, R.; Kraus, P. Following the Nonthermal Phase Transition in Niobium Dioxide by Time-Resolved Harmonic Spectroscopy. *Physical Review Letters* **2023**, *131*, 243201.

(20) Zhang, J.; Wang, Z.; Lengers, F.; Wigger, D.; Reiter, D. E.; Kuhn, T.; Wörner, H. J.; Luu, T. T. High-harmonic spectroscopy probes lattice dynamics. *Nature Photonics* **2024**, *18*, 792–798.

(21) Lemieux, S.; Jalil, S. A.; Purschke, D. N.; Boroumand, N.; Hammond, T. J.; Vil-leneuve, D.; Naumov, A.; Brabec, T.; Vampa, G. Photon bunching in high-harmonic emission controlled by quantum light. *Nature Photonics* **19**, 767–771.

(22) Huang, T.; Zhu, X.; Li, L.; Liu, X.; Lan, P.; Lu, P. High-order-harmonic generation of a doped semiconductor. *Physical Review A* **2017**, *96*, 043425.

(23) Yu, C.; Hansen, K. K.; Madsen, L. B. Enhanced high-order harmonic generation in donor-doped band-gap materials. *Physical Review A* **2019**, *99*, 013435.

(24) Sivis, M.; Taucer, M.; Vampa, G.; Johnston, K.; Staudte, A.; Naumov, A. Y.; Vil-leneuve, D. M.; Ropers, C.; Corkum, P. B. Tailored semiconductors for high-harmonic optoelectronics. *Science* **2017**, *357*, 303–306.

(25) Nefedova, V. E. et al. Enhanced extreme ultraviolet high-harmonic generation from chromium-doped magnesium oxide. *Applied Physics Letters* **2021**, *118*, 201103.

(26) Korolev, V.; Sinelnik, A. D.; Rybin, M. V.; Lazarenko, P.; Kushchenko, O. M.; Glukhenkaya, V.; Kozyukhin, S.; Zuerch, M.; Spielmann, C.; Pertsch, T.; Staude, I.; Kartashov, d. Tunable high-order harmonic generation in GeSbTe nano-films. *Nanophotonics* **2024**, *13*, 3411–3419.

(27) Elliott, S. R. Medium-range structural order in covalent amorphous solids. *Nature* **1991**, *354*, 445–452.

(28) Sørensen, S. S.; Biscio, C. A. N.; Bauchy, M.; Fajstrup, L.; Smedskjaer, M. M. Revealing hidden medium-range order in amorphous materials using topological data analysis. *Science Advances* **2020**, *6*, eabc2320.

(29) Lan, S. et al. A medium-range structure motif linking amorphous and crystalline states. *Nature Materials* **2021**, *20*, 1347–1352.

(30) Vampa, G.; McDonald, C.; Orlando, G.; Klug, D.; Corkum, P.; Brabec, T. Theoretical Analysis of High-Harmonic Generation in Solids. *Physical Review Letters* **2014**, *113*, 073901.

(31) Floss, I.; Lemell, C.; Wachter, G.; Smejkal, V.; Sato, S. A.; Tong, X.-M.; Yabana, K.; Burgdörfer, J. *Ab initio* multiscale simulation of high-order harmonic generation in solids. *Physical Review A* **97**, 011401.

(32) Abadie, C. Q.; Wu, M.; Gaarde, M. B. Spatiotemporal filtering of high harmonics in solids. *Optics Letters* **43**, 5339.

(33) Orlando, G.; Ho, T.-S.; Chu, S.-I. Simple model of dephasing for high-order harmonic generation in solids. *37*, 1540.

(34) Heide, C.; Kobayashi, Y.; Johnson, A. C.; Liu, F.; Heinz, T. F.; Reis, D. A.; Ghimire, S. Probing electron-hole coherence in strongly driven 2D materials using high-harmonic generation. *Optica* **9**, 512.

(35) Brown, G. G.; Jiménez-Galán, A.; Silva, R. E. F.; Ivanov, M. Real-space perspective on dephasing in solid-state high harmonic generation. *Physical Review Research* **2024**, *6*, 043005.

(36) Molinero, E. B.; Amorim, B.; Ivanov, M.; Brown, G. G.; Cistaro, G.; Lopes, J. a. M. V. P.; Jiménez-Galán, A.; San-Jose, P.; Silva, R. E. F. Semiconductor Wannier equations: a real-time, real-space approach to the nonlinear optical response in crystals (ATATA). *arXiv:2510.22064*

(37) You, Y. S.; Reis, D.; Ghimire, S. Anisotropic high-harmonic generation in bulk crystals. *Nature Physics* **2017**, *13*, 345–349.

(38) Langer, F.; Hohenleutner, M.; Huttner, U.; Koch, S. W.; Kira, M.; Huber, R. Symmetry-controlled temporal structure of high-harmonic carrier fields from a bulk crystal. *Nature Photonics* **2017**, *11*, 227–231.

(39) Suthar, P.; Trojánek, F. s.; Malý, P.; Derrien, T. J.-Y.; Kozák, M. Role of Van Hove singularities and effective mass anisotropy in polarization-resolved high harmonic spectroscopy of silicon. *Communications Physics* **2022**, *5*, 288.

(40) Tauc, J. Optical properties and electronic structure of amorphous Ge and Si. *Materials Research Bulletin* **1968**, *3*, 37–46.

(41) Kramer, B. Electronic structure and optical properties of amorphous germanium and silicon. *Physica Status Solidi (b)* **1971**, *47*, 501–510.

(42) Bose, S. K.; Winer, K.; Andersen, O. K. Electronic properties of a realistic model of amorphous silicon. *Physical Review B* **1988**, *37*, 6262–6277.

(43) Tamura, M.; Shukuri, S.; Moniwa, M.; Default, M. Focused ion beam gallium implantation into silicon. *Applied Physics A Solids and Surfaces* **1986**, *39*, 183–190.

(44) Winkler, F.; Strobel, C.; Wenzel, C.; Bartha, J. W. The Doping of Si p-Field-Effect Transistor Devices by Gallium Focused Ion Beam Implantation Enabling Flexible Fabrication Routes at Moderate Temperatures. *Physica Status Solidi (a)* **2021**, *218*, 2000511.

(45) Drezner, Y.; Greenzweig, Y.; Tan, S.; Livengood, R. H.; Raveh, A. High resolution TEM analysis of focused ion beam amorphized regions in single crystal silicon—A complementary materials analysis of the teardrop method. *Journal of Vacuum Science & Technology B, Nanotechnology and Microelectronics: Materials, Processing, Measurement, and Phenomena* **2017**, *35*, 011801.

(46) Korobenko, A.; Rashid, S.; Naumov, A. Y.; Villeneuve, D. M.; Reis, D. A.; Berini, P.; Corkum, P. B.; Vampa, G. In situ high-harmonic microscopy of a nanostructured solid. *Optica* **2023**, *10*, 642.

(47) Cocker, T. L.; Baillie, D.; Buruma, M.; Titova, L. V.; Sydora, R. D.; Marsiglio, F.; Hegmann, F. A. Microscopic origin of the Drude-Smith model. *Physical Review B* **2017**, *96*, 205439.

(48) Purschke, D. N.; Pielmeier, M. R. P.; Üzer, E.; Ott, C.; Jensen, C.; Degg, A.; Vogel, A.; Amer, N.; Nilges, T.; Hegmann, F. A. Ultrafast Photoconductivity and Terahertz Vibrational Dynamics in Double-Helix SnIP Nanowires. *Advanced Materials* **2021**, *33*, 2100978.

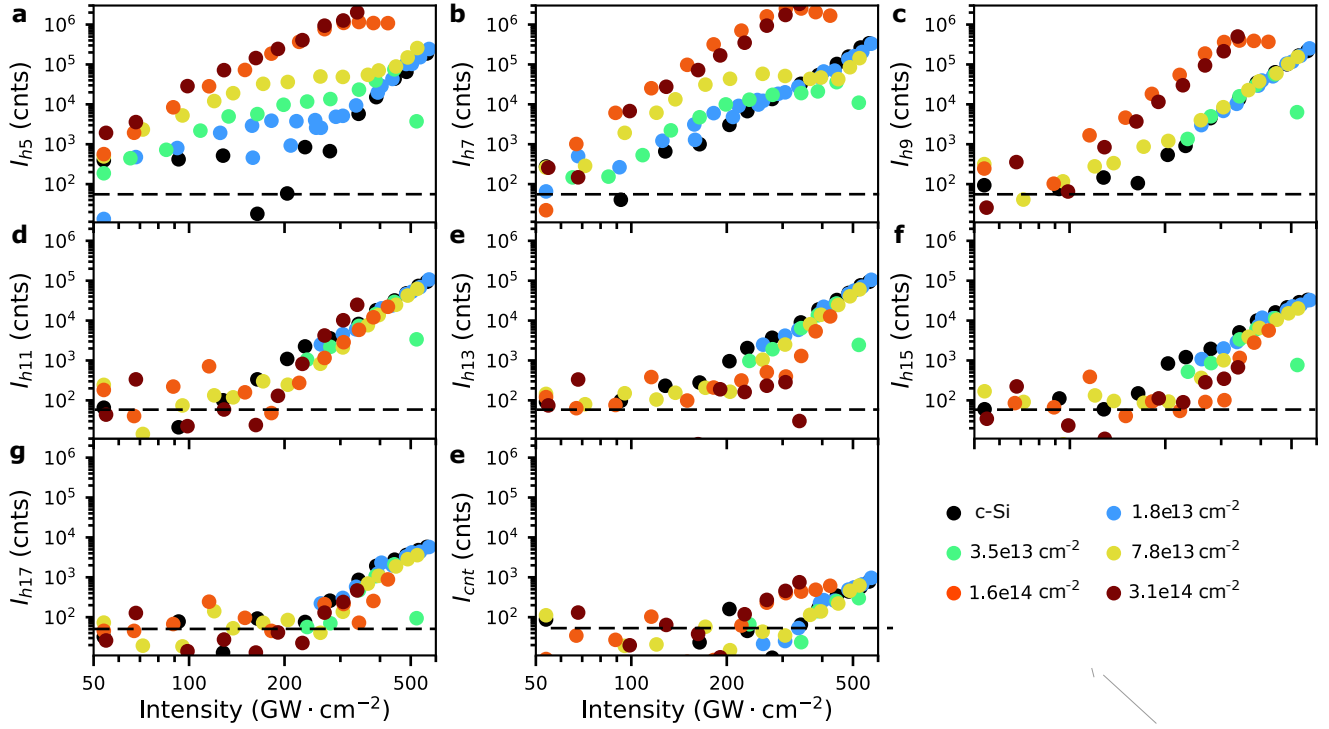
(49) Alexander, O.; Barnard, J. C. T.; Larsen, E. W.; Avni, T.; Jarosch, S.; Ferchaud, C.; Gregory, A.; Parker, S.; Galinis, G.; Tofful, A.; Garratt, D.; Matthews, M. R.; Marangos, J. P. Observation of recollision-based high-harmonic generation in liquid isopropanol and the role of electron scattering. *Physical Review Research* **2023**, *5*, 043030.

(50) Mondal, A.; Neufeld, O.; Yin, Z.; Nourbakhsh, Z.; Svoboda, V.; Rubio, A.; Tancogne-Dejean, N.; Wörner, H. J. High-harmonic spectroscopy of low-energy electron-scattering dynamics in liquids. *Nature Physics* **2023**, *19*, 1813–1820.

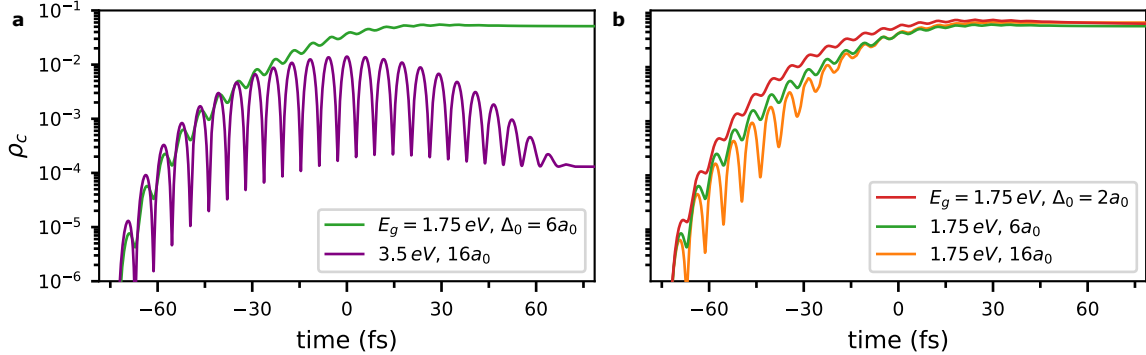
(51) Purschke, D. N.; Korobenko, A.; Staudte, A.; Naumov, A. Y.; Villeneuve, D. M.; Vampa, G. Inline-delay Fourier transform imaging spectrometer for mid-IR ultrashort pulses. *Optics Express* **2024**, *32*, 37635.

(52) Pierce, D. T.; Spicer, W. E. Electronic Structure of Amorphous Si from Photoemission and Optical Studies. *Physical Review B* **1972**, *5*, 3017–3029.

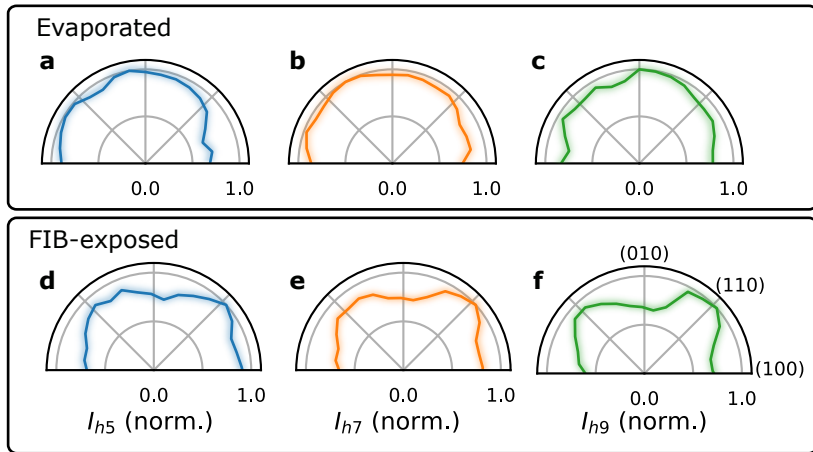
## Extended data



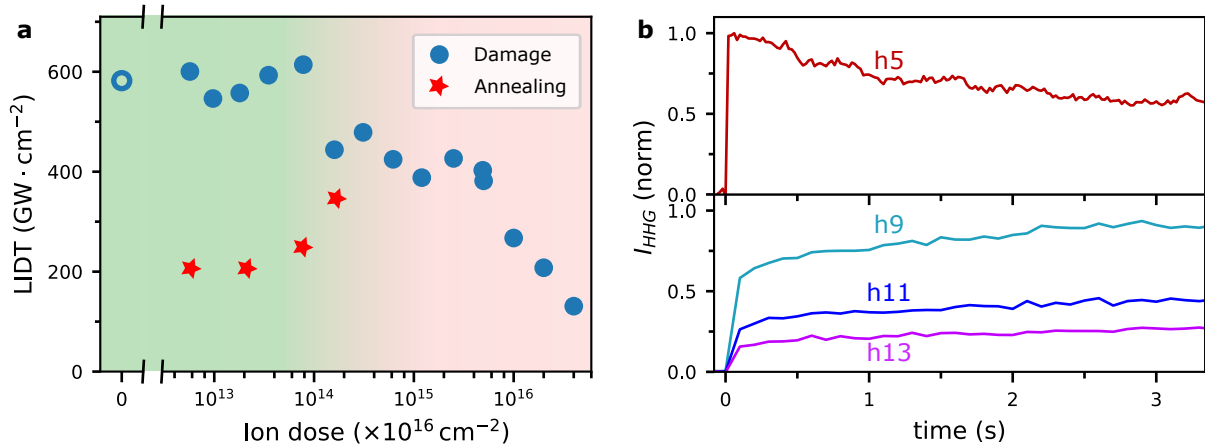
**Extended Data Fig. 1:** **a-g**, Yield of harmonics h5-h17, respectively, as a function of peak laser intensity for samples with Ga dose ranging from  $3.5-120 \times 10^{13} \text{ cm}^{-2}$ . **h**, Continuum/noise background as a function of laser intensity. Black dashed lines: noise level.



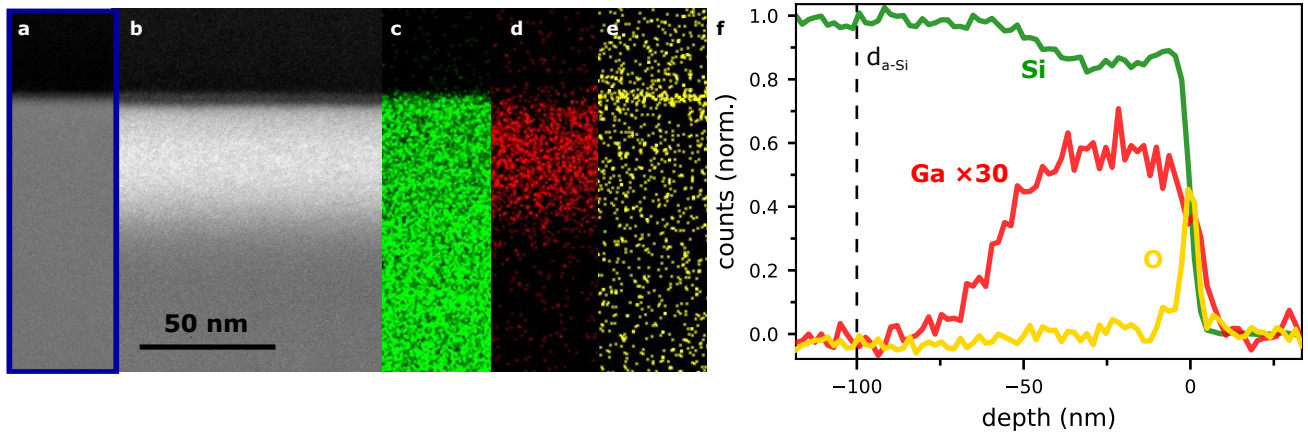
**Extended Data Fig. 2:** Log-scaled time-dependent conduction band population for the same parameters as **a** Fig. 2h and **b**, Fig. 2g.



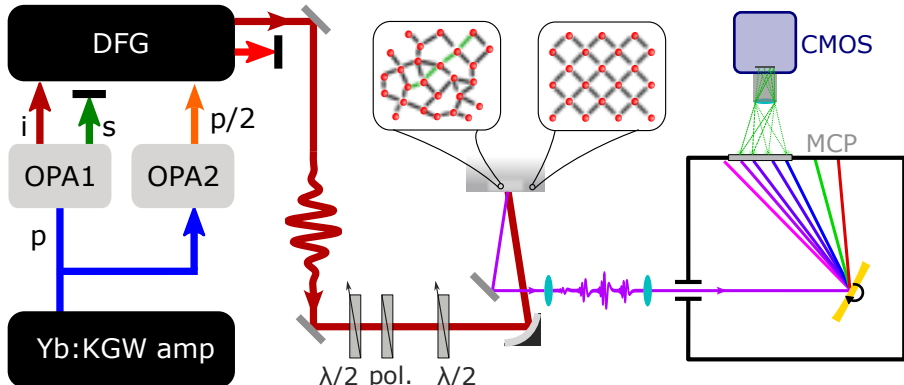
**Extended Data Fig. 3:** **a-c**, Polar plot of the yields of h5-h9, respectively, for an a-Si film deposited by e-beam evaporation. **d-f**, Polar plot of the yields of h5-h9, respectively, for a FIB film amorphized with a  $6.2 \times 10^{15} \text{ cm}^{-2}$  dose of Ga ions. The FIB-amorphized films display remnant cubic structure while the a-Si film deposited by evaporation are more isotropic. The lack of polarization dependence in the evaporated films does not, by itself, mean there is no medium-range order, simply that there is no preferred alignment.



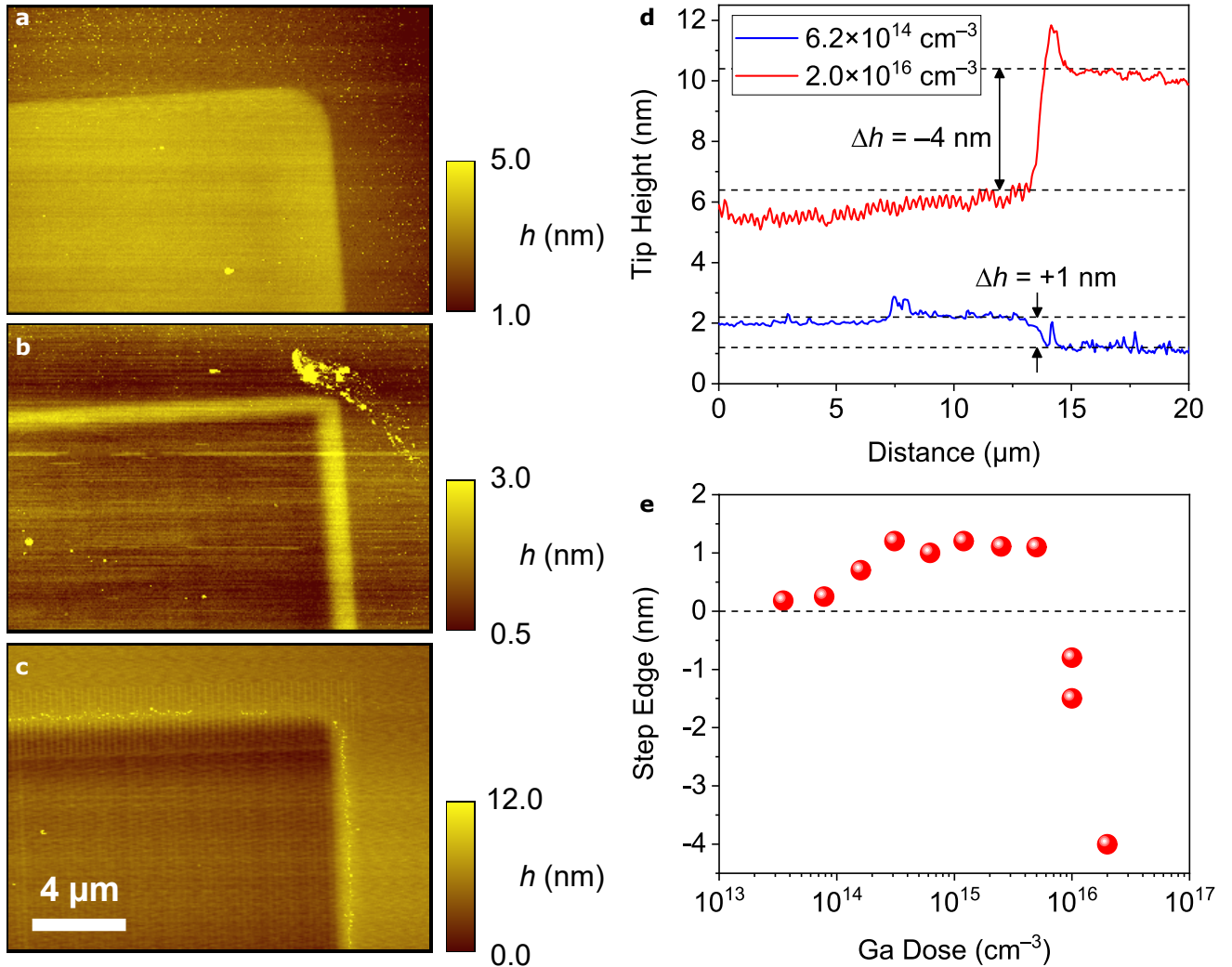
**Extended Data Fig. 4:** **a**, LIDT for all ion doses (blue circles) and approximate laser annealing threshold for several samples below the critical dose (red stars). The green to red coloring indicates the approximate critical dose based on literature and HHG. While roughly constant up to the critical dose ( $\sim 10^{14} \text{ cm}^{-2}$ ), the LIDT suddenly drops above it. At higher doses, above ( $\sim 5 \times 10^{15} \text{ cm}^{-2}$ ), the damage threshold begins to drop significantly with increasing dose. This is correlated with the dose at which we begin to observe significant etching of the Si surface (see Extended data Fig. 7). **b**, Time-dependent yield of harmonic generation while annealing. Data for the top plot (h5) was measured on a Thorcam and data for the bottom plot was measured in the UV spectrometer described previously. The ion dose for this sample was  $210 \text{ GW} \cdot \text{cm}^{-2}$ . We observe a decrease in the yield of h5 over a timescale of several seconds as well as an increase in the yields of h9-h13.



**Extended Data Fig. 5:** Dark-field images of **a**, a Ga-implanted region with an ion dose of  $4 \times 10^{16} \text{ cm}^{-2}$  and **b**, a bare sample (no implantation) in the vicinity of the surface. Elemental profile map for Si **c**,, Ga **d**,, and O **e**. **f**, Depth profile of taken from the images in **c-e**,. The black vertical line indicates the location of the a-Si/c-Si boundary as determined from CBED. Note the high Ga dose ( $400\times$  greater than the critical dose) was chosen for EDS profiling to ensure a sufficiently high concentration to resolve the Ga. At this high dose, we observe a measureable reduction in the Si signal, however, at the critical dose we expect a much smaller Ga concentration of only  $1.4 \times 10^{19} \text{ cm}^{-3}$  (0.03% fractional doping).



**Extended Data Fig. 6:** Experimental apparatus as described in the Methods. OPA architecture: an Yb laser (1030 nm) pumps a dual OPA, one degenerate (OPA2) and one non-degenerate (OPA2). The signal from OPA1 is amplified by the output of OPA1 to yield short pulses at  $3.6 \mu\text{m}$ . The intensity is controlled by a hal waveplate/polarizer combination and a second half wave plate is used for polarization sensitive measurements. The laser is focused onto the sample at near normal incidence using an off-axis parabolic mirror. The harmonics are collected and directed into a home-built UV spectrometer consisting of a curved grating and intensifier, which is imaged using a CMOS camera.

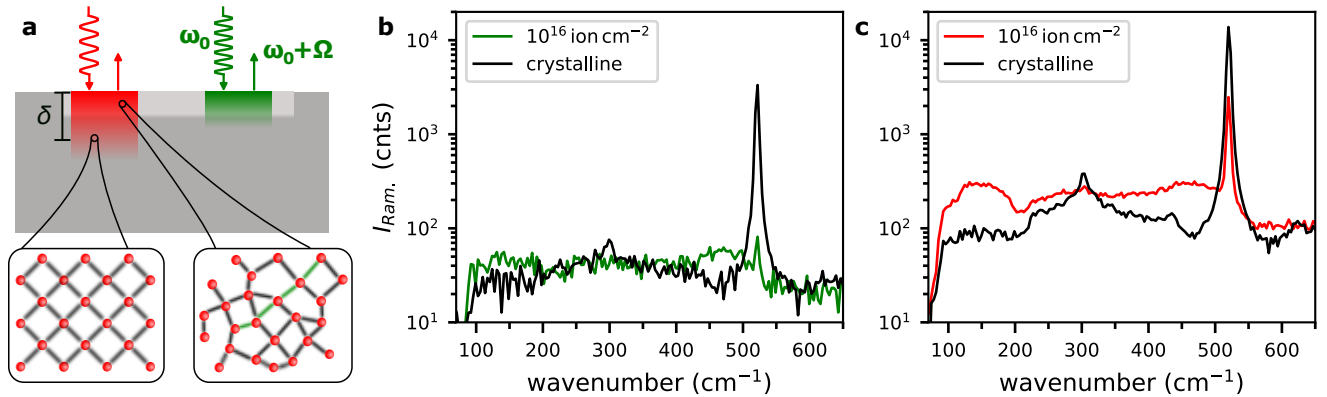


**Extended Data Fig. 7:** Atomic-force microscope (AFM) of FIB patterned a-Si regions with Ga doses of **a**,  $0.5 \times 10^{15} \text{ cm}^{-2}$ , **b**,  $1 \times 10^{16} \text{ cm}^{-2}$ , and **c**,  $2 \times 10^{16} \text{ cm}^{-2}$ . **d**, Line scans of the surface topography for two different samples, showing the step-edge etching in the high-dose regime and swelling in the low-dose regime. **e**, Step-edge height as a function of Ga dose. The 1 nm surface swelling is consistent with expectation based on the relative densities of a-Si and c-Si.

# Supplementary Information

## Raman spectroscopy

Spectra were acquired in a Raman microscope in back-scatter mode with two different laser excitation wavelengths (514 nm and 633 nm), as illustrated in Supplementary Fig. 1a. The corresponding spectra for each laser are shown in Supplementary Figs. 1b and c, respectively. In both cases, the amplitude of the sharp LO peak is greatly reduced in the amorphous phase relative to c-Si, however, relative to the broad a-Si Raman peaks, the sharp LO peak is much stronger with the 633 nm laser and hardly present with the 514 nm laser. The signal strength is also significantly lower for the 514 nm laser than the 633 nm laser.



**Supplementary Fig. 1:** **a**, Illustration of the Raman backscatter geometry and the penetration depth,  $\delta$ , for the two different lasers. The schematics indicate the crystalline and amorphous regions of the sample. The a-Si film thickness is approximately 65 nm. Raman spectra of c-Si (black) and a-Si measured with **b**, a 514 nm excitation wavelength, and **c**, a 633 nm excitation wavelength.

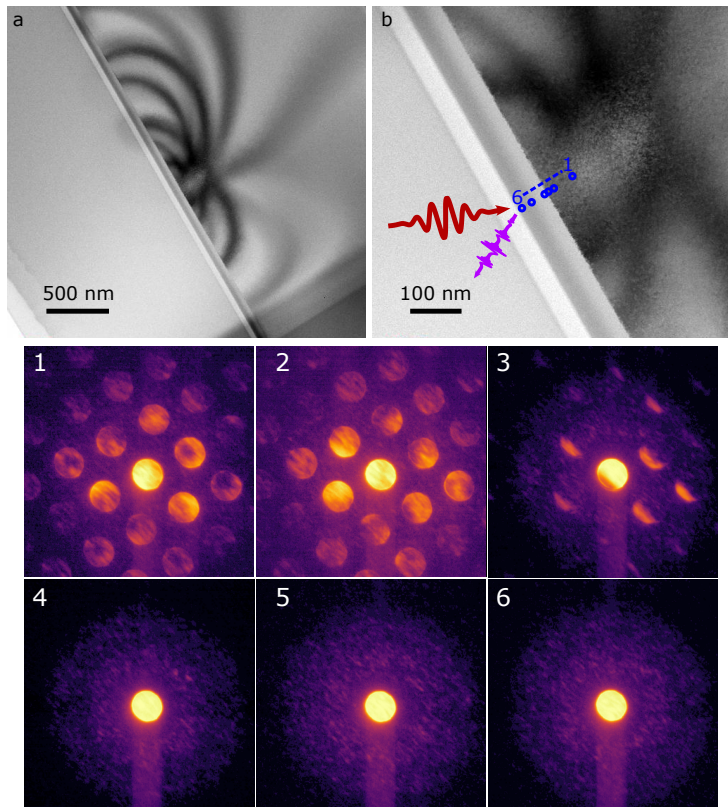
As illustrated in Supplementary Fig. 1a, due to the longer wavelength (and corresponding lower absorption coefficient<sup>40</sup>), the 633 nm laser can penetrate deeper into the c-Si substrate (recall the 65 nm a-Si film thickness measured by TEM). Thus, the c-Si peak is more prominent for longer-wavelength excitation. This effect is two-fold: reabsorption of emission from the c-Si substrate also stronger for the shorter-wavelength excitation. As a result, Raman spectra from the 514 nm laser are more selective to the a-Si thin film than with the 633 nm laser. The dramatically reduced sharp LO peak strength relative to the broad a-Si peak

therefore suggests that it arises from the c-Si substrate. We emphasize that for HHG spectroscopy, we do not need to perform such careful analysis to verify the that the origin of the signal is in the a-Si layer: because the low-order harmonics are enhanced by FIB treatment, this emission must originate in the a-Si layer.

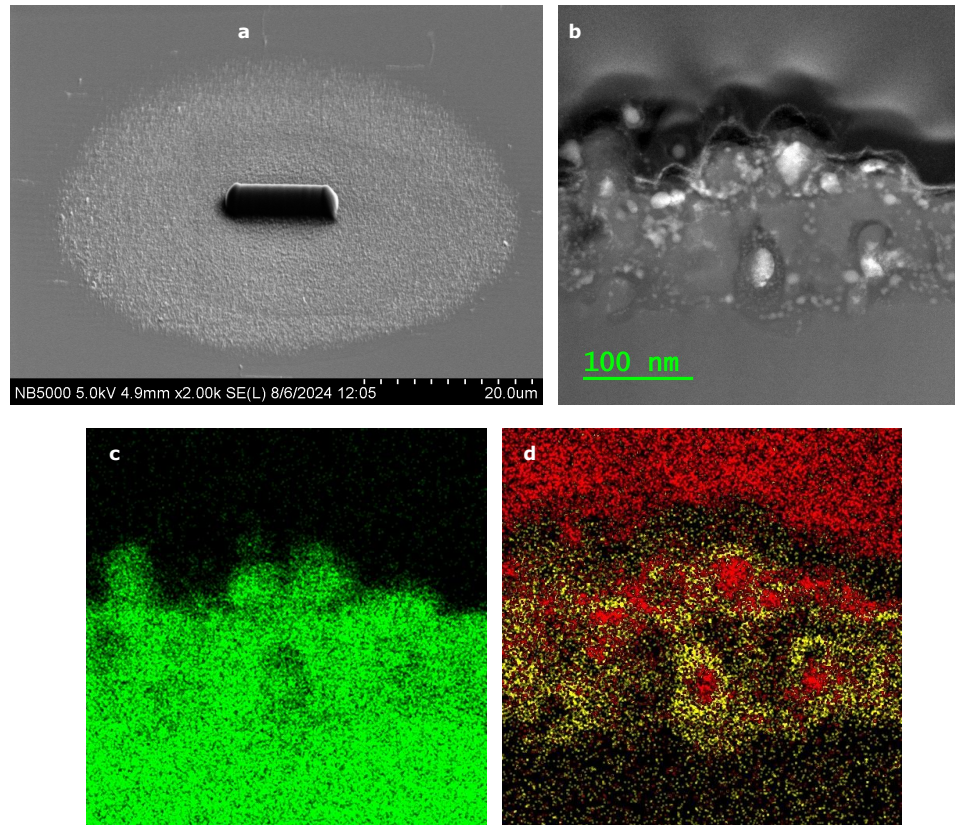
## Supplementary TEM and EDS data

**Additional TEM and CBED images.** A large TEM image of the lamella described in the main text is shown in Supplementary Fig. 2a. The Kikuchi pattern, with curved lines due to the warping of the Si lamella, points towards the region of correct orientation for HR-TEM and CBED analysis. A magnified image of this region is shown in Supplementary Fig. 2b. A schematic image of the laser pulse propagation directions is superimposed on this image. CBED patterns were acquired from the blue circled regions and plotted with log-scaled colormaps in Supplementary Figs. 21-6. Here, we see one CBED pattern, taken precisely at the a-Si/c-Si interfaces, shows a diffraction pattern with mixed character of both the ordered and disordered structure.

We performed EDS analysis on a laser damage spot on the a-Si film. Shown in Supplementary Fig. 3 is a scanning electron microscope image of the laser damage spot with the lamella milled out by FIB, as described in the methods. A TEM cross section of the lamella is shown in Supplementary Fig. 3b. Several bright spots are clearly visible in the image, in Supplementary Fig. 3c-d, we plot elemental profiles of the Si and an overlay of the Ga and O, respectively. The hotspots in the TEM image correspond to the formation of Ga-rich nanocrystals. Additionally, we see a significant amount of O penetrated into the film, which could indicate that the damaged a-Si film has increased porosity. The laser damage also induces corrugations in the surface approximately 100 nm deep at the interface with the bulk Si. This is larger than the 65 nm thickness of the a-Si layer estimated from TEM and CBED, which could be due to the increased porosity reducing the density, however, this requires more investigation.



**Supplementary Fig. 2:** **a**, Large-scale TEM cross section of a lamella extracted from a sample with Ga ion dose  $4 \times 10^{16} \text{ cm}^{-2}$ , highlighting the Kikuchi patterns in the c-Si substrate. **b**, Zoomed in image of the sample in **a**, focused on the region with the correct orientation for electron diffraction. The 6 blue circles indicate the regions where CBED was performed. **1-6**, Log-scaled image of the CBED patterns for the regions circled in **a**.



**Supplementary Fig. 3:** **a**, SEM image of a spot damaged by the IR laser on a sample with Ga ion dose  $4 \times 10^{16} \text{ cm}^{-2}$ . The dark rectangular spot in the middle is the lamella that was milled out for elemental analysis. **b**, TEM image of a cross section of the lamella and elemental EDS profiles taken at **c**, the Si edge and **d**, an overlay of the Ga (red) and O (yellow) edges.

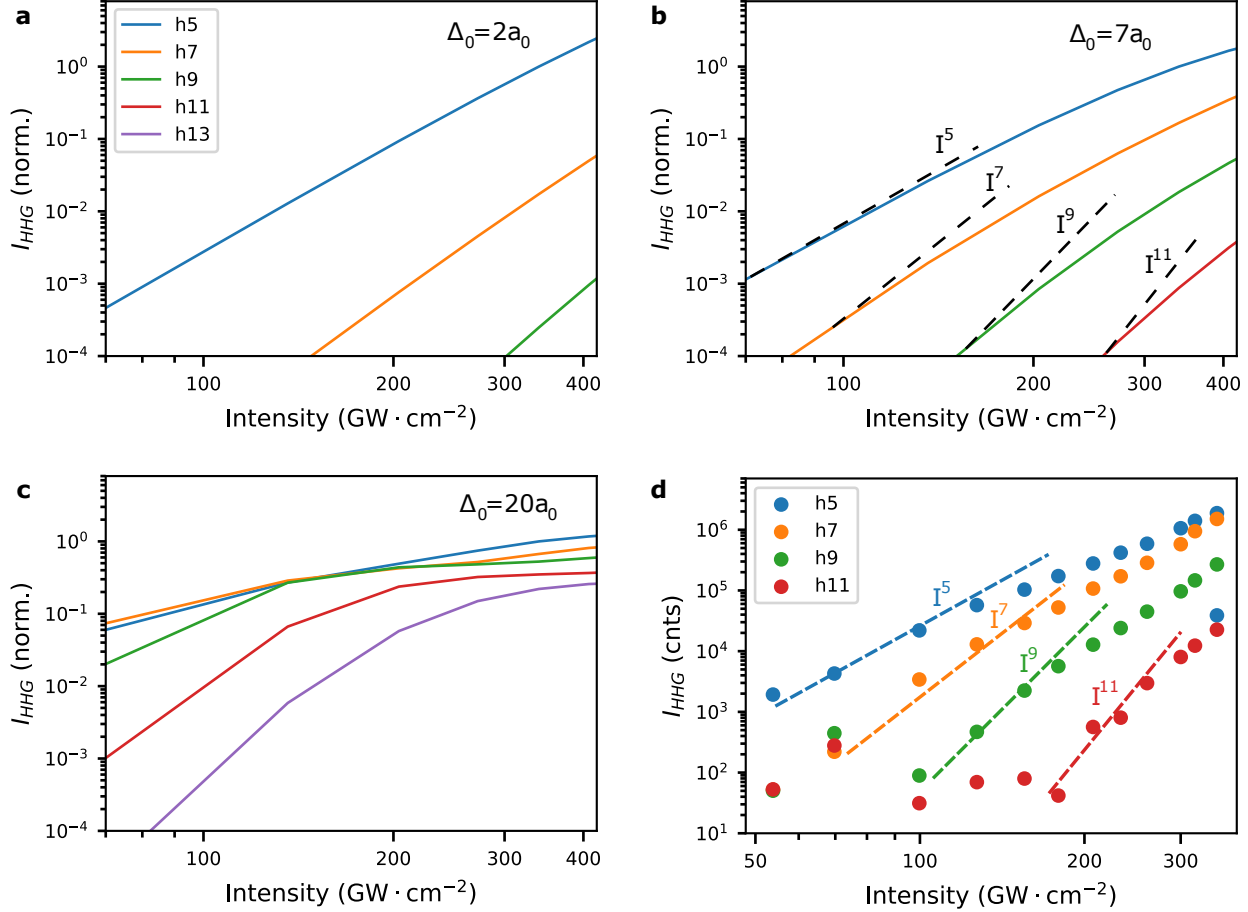
## Role of real-space dephasing in quantum dynamics

In this Supplementary section we explore the role of real-space dephasing in quantum dynamics, specifically, how it affects the calculated HHG spectra. Briefly, it is split into three parts: In the first, we show how  $\Gamma_{RS}$  affects the scaling of HHG yield with the peak intensity of the driving laser, which provides a secondary piece of information for guiding the estimate of the length scale of medium-range order. Second, we show how the (approximate) insensitivity of the HHG plateau to the peak-intensity of the driving laser in the strong-field regime is beneficial to the the estimated scale of medium-range order. Third, we show how the calculated spectra are insensitive to the curvature of  $\Gamma_{RS}$  only if the location of the dephasing boundary,  $\Delta_0$  as defined in the main text, is chosen correctly.

**Intensity scaling of harmonic yield.** Here, we study the HHG yield as a function of driving laser intensity in calculation in comparison to the experimentally measured values. As shown in Supplementary Figs. 4a-c, the functional form of the intensity dependence is highly sensitive to the location of the dephasing boundary. The experimentally measured intensity scaling is plotted in Supplementary Fig. 4d. None of the harmonics scale perturbatively, i.e., experimentally we are in the non-perturbative regime of light-matter interaction. In the calculations when the dephasing boundary is significantly larger than the expected maximum excursion length ( $8a_0$ , Supplementary Fig. 4c), the harmonics show clear non-perturbative scaling and at high intensity, their yields begin to saturate, i.e., we observe a plateau. Moving the dephasing boundary inwards (Supplementary Figs. 4a-b), the scaling of harmonics becomes closer to perturbative ( $I_{hn} \propto I^n$ ).

The sensitivity of the intensity scaling of HHG yields to  $\Gamma_{RS}$  point to an alternative metric for gauging the length-scale of medium-range order. The experimentally-measured scaling is most similar to that of the calculations with dephasing boundary  $\Delta_0 \sim 7a_0$ . Due to the broad bandwidth of the harmonic spectrum, macroscopic effects, response curves of detectors, and reflectivity/transmission of optics make determination of the absolute yield in an HHG experiment challenging. Intensity scaling, which is a relative measurement, is

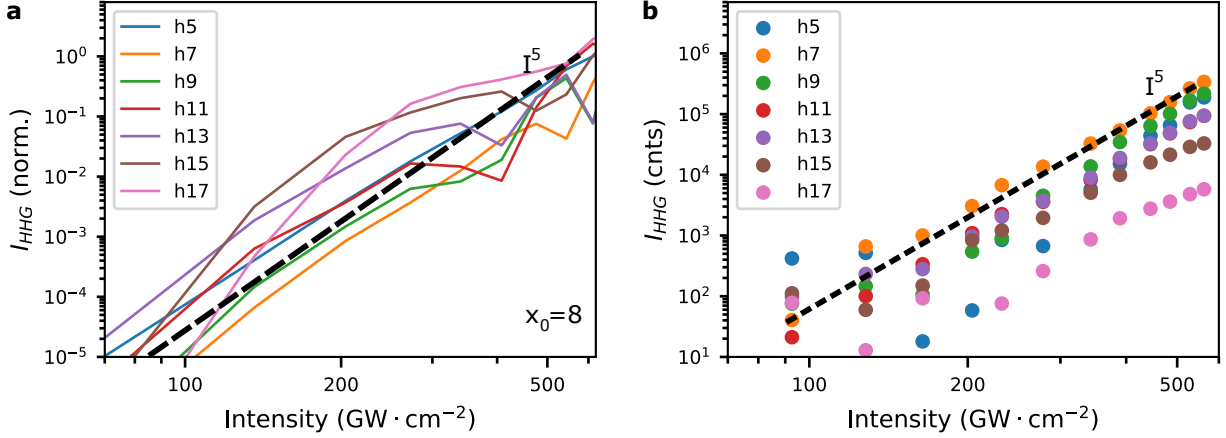
not affected by these artifacts, thus, it provides a helpful validation of the length scale of medium-range order estimated from the roll off in the spectra.



**Supplementary Fig. 4:** Peak amplitude of several harmonic orders as calculated in the 2-band model as a function of intensity with real-space dephasing boundaries at **a**,  $\Delta_0 = 2a_0$ , **b**,  $\Delta_0 = 7a_0$ , and **c**,  $\Delta_0 = 20a_0$ . In **b**, the dashed black lines represent perturbative scaling laws with  $I_{hn} \propto I^n$ . **d**, Experimentally measured scaling of the harmonic yield in a-Si with an ion dose of  $6.2 \times 10^{14} \text{ cm}^{-2}$ .

We also report the intensity scaling of HHG from the 2-band model for c-Si, shown in Supplementary Fig. 5a, and in experiment, shown in Supplementary Fig. 5b. In the experimental data, all harmonic orders scale with  $\sim I^5$ . The highest order harmonics (h15-h17) show signs of plateauing at the highest intensities. Despite the simplicity of the 1D 2-band model, these trends are roughly followed by the calculation. With the exception of h15 and h17, all harmonics show  $\sim I^5$  scaling; h15 and h17 show sharper scaling at low intensity, however, only below  $200 \text{ GW} \cdot \text{cm}^{-2}$  where the SNR in the experimental data is

low. Above  $300 \text{ GW} \cdot \text{cm}^{-2}$ , the higher-order harmonics begin to oscillate with intensity in calculations. These oscillations are not apparent in the experimental data, which could be due to focal averaging.



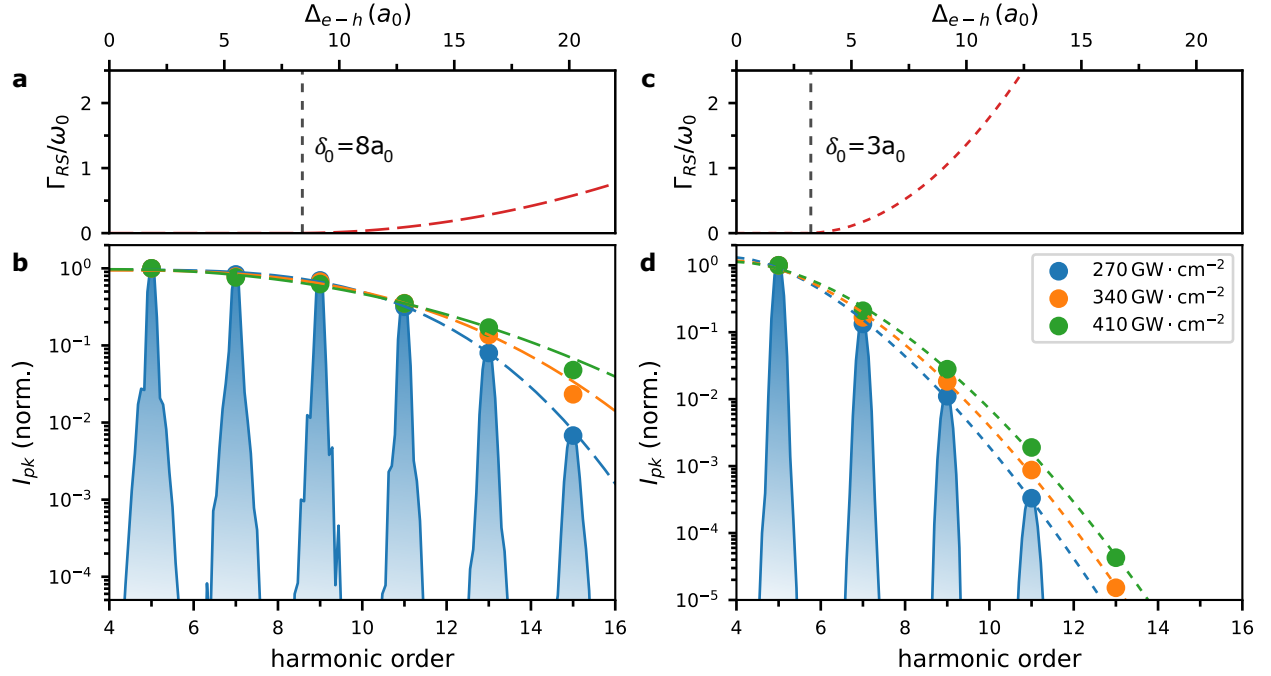
**Supplementary Fig. 5:** **a**, Intensity dependence of the harmonic yield in the 2-band model for c-Si with a real-space dephasing boundary at  $8a_0$ . **b**, Experimentally measured intensity dependence of harmonic yield in c-Si. In both cases, the black dashed line indicates an  $I^5$  scaling law.

**Insensitivity of harmonic roll-off to intensity in the strong-field regime.** Shown in Supplementary Fig. 6b is the peak amplitude of HHG as a function of harmonic order for three different intensities and a real-space dephasing as shown in Fig. 6a. This boundary is located far enough that the harmonic yield is unaffected but close enough to damp unphysical coherences and clean up the HHG spectra, i.e., it is suitable for an ordered crystal. Because we are in the strong-field regime, the normalized HHG spectra are relatively insensitive to the laser intensity. This is intrinsically related to the non-perturbative regime of light-matter interaction, where a harmonic plateau is formed. This insensitivity to intensity is, to some extent, carried over to the calculations for a disordered solid, with a  $\Gamma_{RS}$  shown in Fig. 6c and the HHG spectra shown in Fig. 6d. Note that due to the rather large nonlinearity ( $\sim I^5$  scaling), a change in intensity by a factor of 1.5 corresponds to an increase in yield of nearly 8 times. Clearly, the non-perturbative regime of light-matter interaction is crucial for this estimate. Note, the dashed lines are phenomenological fits to a stretched exponential

function of the form,

$$I(E_n) \propto \exp\left(-\frac{(E_n - E_g)^\beta}{\tau^\beta}\right), \quad (7)$$

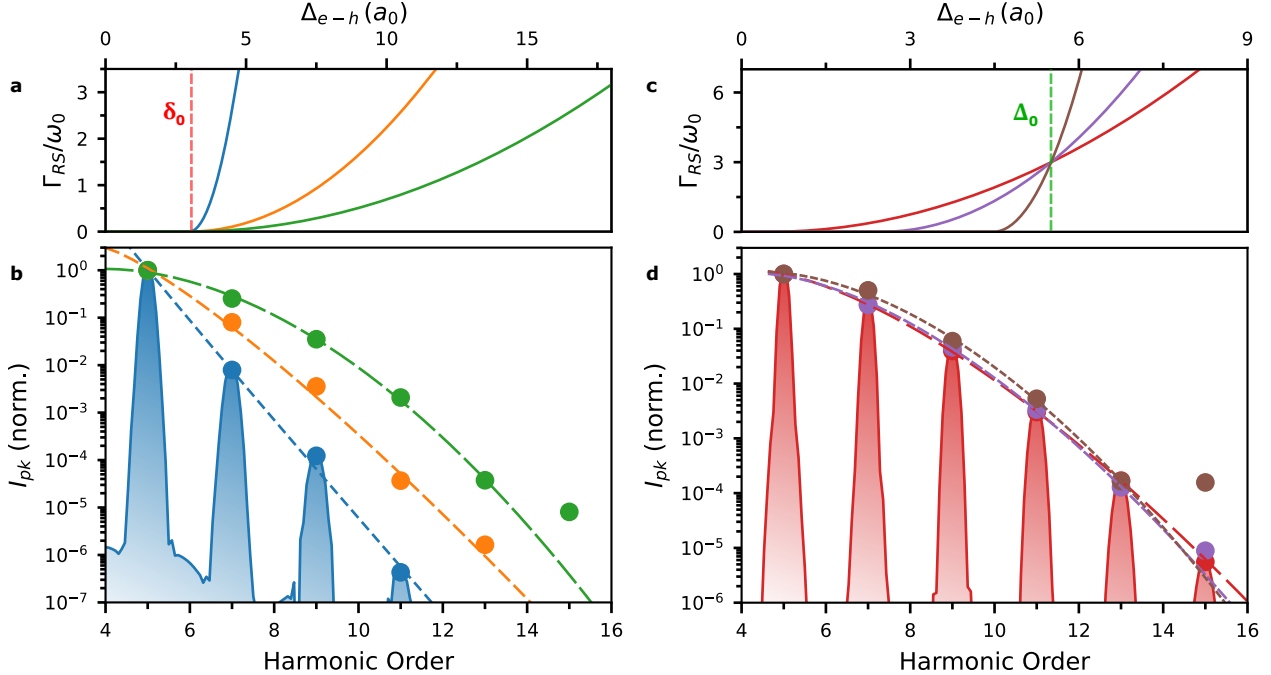
where  $\beta$  and  $\tau$  are fit parameters.



**Supplementary Fig. 6:** **a**,  $\Gamma_{RS}$  with  $\delta_0 = 8a_0$ , i.e., for an ordered structure. **b**, Calculated HHG yield of the harmonics for several different intensities using the functional form for  $\Gamma_{RS}$  in **a**. **c**,  $\Gamma_{RS}$  with  $\delta_0 = 3a_0$ , i.e., for a disordered structure. **d**, Calculated HHG yield of the harmonics for several different intensities using the functional form for  $\Gamma_{RS}$  in **c**. In **b**, and **d**, the blue shaded region indicates the calculated HHG spectrum for an intensity of  $270 \text{ GW} \cdot \text{cm}^{-2}$ . For clarity, only the peak amplitudes are plotted for all intensities (colored circles). The solid lines are fits to a stretched exponential function, drawn as a guide to the eye.

**Choosing the correct dephasing boundary.** As outlined in the methods,  $\Gamma_{RS}$  is parameterized as a second-order polynomial function, which is physically motivated by the expectation that it should be a smooth function. While in the future, we expect the precise functional form to be motivated by theoretical considerations, here we define the polynomial curvature ad hoc. At first glance, this might appear to nullify our ability to estimate the length-scale of medium-range order. Indeed, as shown in Fig. 7a-b, we show that, for a fixed  $\delta_0$ , the spectra are highly sensitive to the curvature.

However, this simply shows that  $\delta_0$  is poor choice of definition for the dephasing boundary. Instead, as we show in Fig. 7c-d, if we use  $\Delta_0$ , i.e., the e-h separation where the scattering rate reaches  $3\omega_0$ , only the fine structure of the calculated spectra is sensitive to the curvature. This can be understood physically, the dephasing rate must be comparable to the inverse trajectory time to effectively eliminate the coherence.



**Supplementary Fig. 7:** **a**, Three different parameterizations of the real-space dephasing boundary,  $\Gamma_{RS}$ , with the fixed point chosen as the edge of the dephasing boundary,  $\delta_0$ , and various slopes,  $\beta$ . **b**, Roll-off in the peak amplitude of harmonics calculated with the real-space dephasing boundaries in **a**, highlighting the sensitivity of the spectra to the slope when the fixed point is  $\delta_0$ . **c**, Parameterization of  $\Gamma_{RS}$  with a fixed-point chosen with a scattering rate of a third of a cycle. The location of this fixed point as  $\Delta_0$ . **d**, Roll-off in the peak amplitude of harmonics calculated  $\Gamma_{RS}$  given by the three curves in **c**. In contrast to the calculations in **d**, the roll-off of the harmonics is insensitive to the parameterization.

**Discussion.** We note that there are several effects that we have not included in our model that are worth discussion. First, while here we use a simple 2-band model, in reality multi-band effects have been shown to be important in solid HHG. In our case, multi-band effects are mitigated by the long wavelength of the excitation laser; all of the harmonics that we measure are within the first conduction band of silicon. Thus, as mentioned in the main text, the mid-infrared wavelength is crucial to our study. Second, the hopping parameter was

chosen based on the band structure of c-Si. We note once again that the electronic structure of a-Si has been studied extensively and has shown that this is a reasonable first approximation, however, error in the hopping parameter—and thus, the effective mass—translates into an error in the length scale estimate. In the future, this issue could be mitigated by simultaneously performing HHG band-structure tomography to find the correct (ensemble averaged) band curvatures.

In general, it is clear that in the future, a more detailed electronic structure model will be required to be more quantitative. We expect significant room for progress in understanding how disorder, be it static—as in amorphous solids—or dynamic—as from phonons and zero-point motion—maps into the decoherence of e/h pairs.